npj | climate and atmospheric science

Article

Published in partnership with CECCR at King Abdulaziz University

https://doi.org/10.1038/s41612-026-01438-0

Drivers of winter Arctic sea ice variability

P. Vaideanu[1,2] ✉, C. Stepanek[1], D. R. Nichita[2,3], M. Dima[1,2], M. Ionita[1] & G. Lohmann[1,4]

Winter Arctic sea ice concentration (SIC) variability reflects both anthropogenic warming and internal climate variability, but separating their Arctic signatures remains difficult. Here, we apply Canonical Correlation Analysis to October–March global sea surface temperature and Arctic SIC, 2-m air temperature (T2M), and sea level pressure fields over 1950–2024, to isolate coupled modes associated with anthropogenic influence, multidecadal and interannual internal variability. The leading pair represents the winter Arctic response to anthropogenic warming, explaining 35% of SIC and 43% of T2M variance, and is characterized by basin-wide SIC loss coupled with increased T2M. The second pair captures a similar but weaker in magnitude multidecadal signal, with the strongest SIC impacts in the Barents–Kara Seas and Baffin Bay. Two additional pairs reflect interannual variability and show dipolar SIC–T2M structures. Causality and physical diagnostics support these attributions, showing mainly thermodynamic coupling for anthropogenic and multidecadal drivers and circulation-driven advection for interannual pairs. Since 1980, Arctic winter SIC decline has been dominated across most sectors by the anthropogenic impact, with additional regional modulation from multidecadal Atlantic variability.

Recognized by the IPCC Sixth Assessment Report[1] as one of the most sensitive indicators of climate change, Arctic sea ice is a defining component of the high-latitude climate system, regulating exchanges of heat, moisture, and momentum between the ocean and atmosphere, and affecting Earth's energy balance. Through its multiple feedbacks, it governs the magnitude of polar amplification[2,3], second in importance only to temperature feedbacks[3,4]. Beyond being a player in climate change at high latitudes, Arctic sea ice decline has been linked to a weakening of the Atlantic Meridional Overturning Circulation[5,6], while its associated shifts in atmospheric circulation can affect the frequency and persistence of extreme events[7,8].

Arctic sea ice decline has been robustly linked to anthropogenic warming, with numerous attribution studies demonstrating a dominant contribution from rising greenhouse gas concentrations[9] to the observed long-term loss of sea ice[10–13]. Superimposed on this forced response is a substantial contribution from internal variability[14–17] via various mechanisms. The positive phase of the Atlantic Multidecadal Oscillation[18] (AMO), associated with anomalously warm North Atlantic SSTs and enhanced poleward heat transport, has been linked to sea ice decline in regions such as the Barents–Kara Seas and Baffin Bay[9,15]. On shorter time scales, atmospheric variability in the North Atlantic modulates sea ice variability by altering storm tracks, surface winds, and the advection of cold and warm air masses, generating pronounced dipolar sea ice anomalies[15,19] through dynamic and advective processes[20–22]. Atmospheric teleconnections from the El Niño–Southern Oscillation (ENSO) also influence Arctic conditions via planetary-wave propagation and modulation of the Aleutian Low[23–25].

Although Arctic sea ice has declined in all seasons, the winter season (here defined as October–March) is of particular physical importance because Arctic amplification is strongest during the cold half of the year[26–29]. In winter, reduced sea ice weakens the insulating effect of the ice and enhances upward ocean-to-atmosphere heat fluxes, promoting strong lower tropospheric warming[2,29]. Sea ice changes also explain a substantial part of the historical winter Arctic surface warming trend, underscoring that winter sea ice is an active component of Arctic amplification rather than merely a passive indicator of climate change[30]. The climatic relevance of winter sea ice also extends beyond local thermodynamic feedbacks, because the atmospheric temperature and energy-budget response to sea ice loss is strongest in winter, even though the largest sea ice losses occur in summer and autumn[31]. At the same time, winter sea ice reflects the combined influence of several interacting factors, including atmospheric circulation, poleward heat and moisture transport, and ocean heat transport into the Arctic[32,33], making it difficult to disentangle the distinct drivers. Furthermore, most previous observational studies of Arctic sea ice variability rely on statistical methods[9,13–16,34] that do not necessarily imply causation, especially in a highly dynamic system such as the Arctic that is shaped by feedbacks, teleconnections, and co-varying influences. To address this hurdle, this study proposes a novel framework for separating the impact of anthropogenic influence from multidecadal and interannual internal variability on winter

[1]Paleoclimate Dynamics, Alfred Wegener Institute Helmholtz Center for Polar and Marine Research, Bremerhaven, Germany. [2]Faculty of Physics, University of Bucharest, Bucharest-Magurele, Romania. [3]"Horia Hulubei" National Institute of Physics and Nuclear Engineering, Bucharest-Magurele, Romania. [4]University of Bremen, Bremen, Germany. ✉e-mail: petru.cosmin.vaideanu@awi.de

Arctic sea ice and associated 2-m air temperature (T2M) and sea level pressure (SLP) patterns by combining Canonical Correlation Analysis[35] (CCA) with two complementary causality techniques, Convergent Cross Mapping[36] (CCM) and Information Flow[37] (IF).

Results

Anthropogenic footprints on Arctic coupled SIC-T2M-SLP fields

To link global climate change to changes in the Arctic, we investigate the co-variability between global SSTs and key Arctic climate fields using CCA, which identifies pairs of spatial patterns ordered based on the correlation between their associated time series (see Methods). The SST pattern of CCA1 (Fig. 1a) explains 40.4% of the variance in this field and displays an almost globally uniform warming structure consistent with long-term anthropogenic radiative forcing. Superimposed on this global signal are the well-known cold anomaly south of Greenland previously linked to anthropogenic influence[38,39], as well as muted warming around Antarctica and localized cooling in the central North Pacific. The corresponding Arctic SIC pattern (35% of variance explained; Fig. 1c) shows a basin-wide reduction in winter SIC, with the strongest negative anomalies extending from the Greenland–Iceland–Norwegian Seas through the Barents–Kara, Laptev, Chukchi, and Beaufort sectors. This spatial structure is consistent with previous observational[9,13] and modeling studies[10,40] regarding the anthropogenic influence on Arctic SIC. The CCA1 T2M pattern (43%; Fig. 1d) is characterized by amplified warming over the exact same regions, while the associated SLP pattern (Fig. 1e) features a weak low-pressure anomaly over the central Arctic and weak positive anomalies over mid-latitudes, a configuration previously linked to anthropogenic warming[41]. The SST-SIC/T2M/SLP time series of CCA1 are significantly correlated ($r = 0.97$; Fig. 1b) and closely track the Global Warming Index (r = 0.94, 95% confidence level). Taken together, the quasi-uniform global SST warming structure, the basin-wide Arctic SIC decline accompanied by amplified T2M warming, and the close correspondence of the canonical time series with the Global Warming Index support the interpretation of CCA1 as the anthropogenically forced mode of Arctic winter variability.

Multidecadal footprints on Arctic coupled SIC-T2M-SLP fields

The SST structure of CCA2 (16.1%; Fig. 2a) is characterized by pronounced positive anomalies in the North Atlantic and negative anomalies over most of the south Atlantic and tropical Pacific. This global-scale pattern has been widely associated with the positive phase of the AMO in both observations[42–44] and climate model simulations[45]. The North Pacific SST pattern, which resembles the negative phase of the Pacific Decadal Oscillation (PDO) and a La Niña-like cooling pattern in the tropical Pacific, is also consistent with previous studies showing that the positive phase of the AMO can induce coherent Pacific SST responses through large-scale atmospheric teleconnections, including modulation of the Aleutian Low and tropical atmospheric bridge mechanisms[42,45,46]. However, the physical origin of the AMO signal itself remains debated, with proposed mechanisms involving ocean circulation[47–49] and external forcing such as aerosols[50], solar variability[51], or volcanic activity[52]. Here, we interpret CCA2 as capturing multidecadal internal variability regardless of its ultimate mechanistic origin. The Arctic SIC pattern of CCA2 (12.4%; Fig. 2c) shows reduced SIC across most of the Arctic, more pronounced over the Barents–Kara Seas and Baffin Bay. This structure is in agreement with previous studies regarding the influence of multidecadal Atlantic variability on Arctic sea ice, in which increased oceanic heat transport into the Nordic Seas, Barents–Kara Seas and Baffin Bay lead to diminished winter sea ice growth[9,32,53–55]. This pattern closely resembles the basin-wide SIC decline identified in the CO_2-dominated CCA1 mode, but with a weaker amplitude. A notable exception is the Fram Strait, where CCA2 displays a slight increase in SIC, indicative of sea ice export from the central Arctic that is associated with AMO[56,57]. The T2M pattern of CCA2 (8.4%; Fig. 2d) is for most regions co-located with changes in sea ice and shows widespread winter warming with maxima over the Barents–Kara Seas and Baffin Bay, regions with the most intense negative

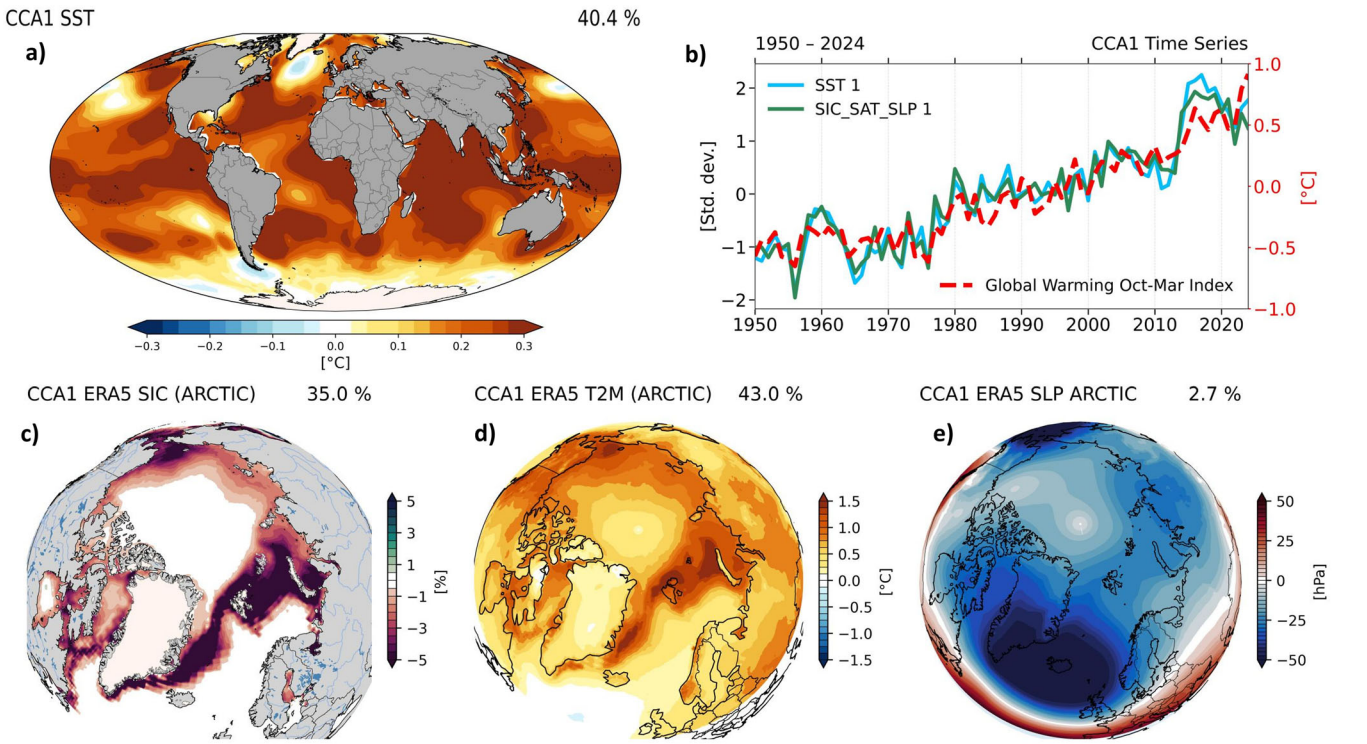

Fig. 1 | First coupled pair of global SST (ERSSTv5) and Arctic SIC, T2M, and SLP (ERA5) October–March anomalies from 1950 to 2024. The SST spatial structure of the first CCA pair (**a**), explaining 40.4% of variance, together with coupled Arctic SIC (**c**; 35% of variance), T2M (**d**; 43% of variance), and SLP (**e**; 2.7% of variance) fields north of 50° N for SIC and T2M, and north of 40° N for SLP. The correlation between their corresponding time series (**b**) is 0.97. Their correlation with Global Warming Index (red line) is 0.94 (95% confidence level).

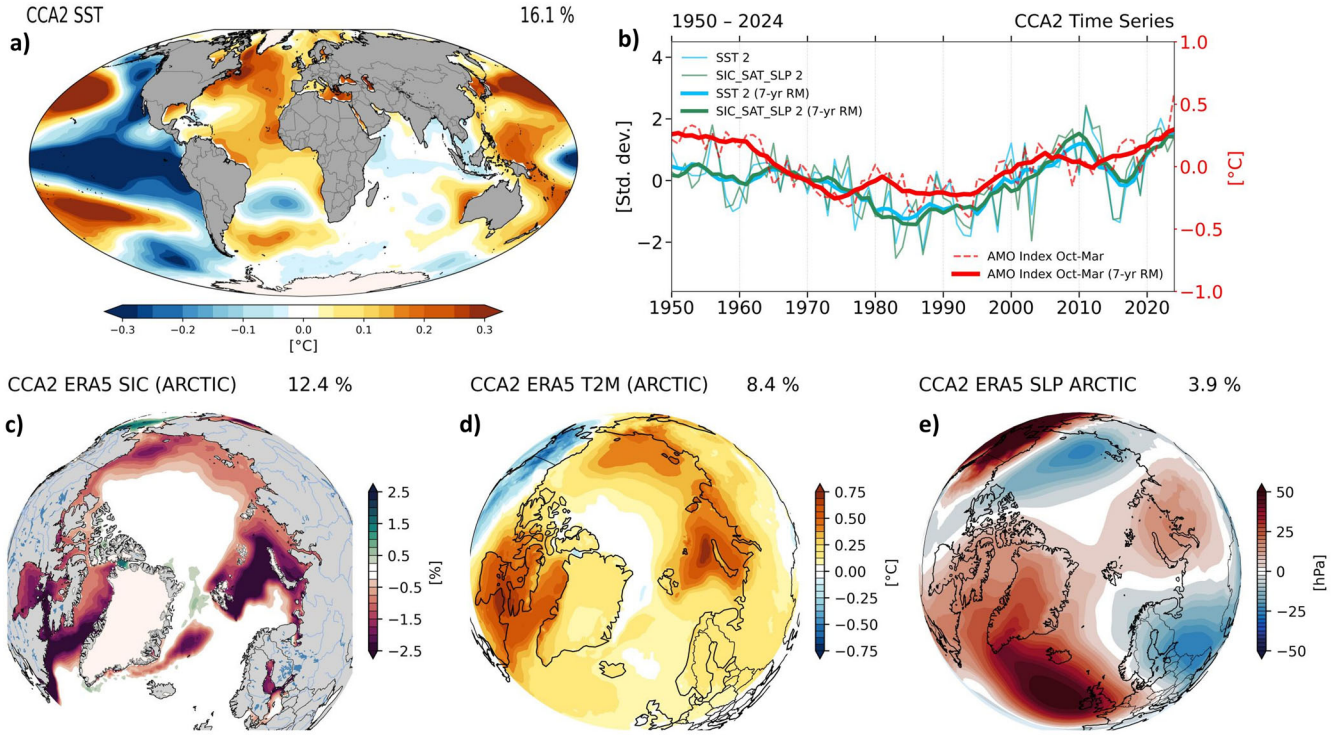

Fig. 2 | Second coupled pair of global SST (ERSSTv5) and Arctic SIC, T2M, and SLP (ERA5) October–March anomalies from 1950 to 2024. The SST spatial structure of the second CCA pair (**a**), explaining 16.1% of variance, together with coupled Arctic SIC (**c**; 12.4% of variance), T2M (**d**; 8.4% of variance), and SLP (**e**; 3.9% of variance) fields north of 50° N for SIC and T2M, and north of 40° N for SLP. The correlation between their corresponding time series (**b**) is 0.93. Their correlation with AMO Index (red line) is 0.45 (95% confidence level).

SIC anomalies. The associated SLP structure (3.9%; Fig. 2e) features positive pressure anomalies over the subpolar North Atlantic and negative-pressure anomalies over the Nordic Seas, favoring sea ice export through Fram Strait[56,57]. The time series for CCA2 (Fig. 2b) exhibits variability on multidecadal timescales that aligns with AMO Index ($r = 0.45$, 95% confidence level). The SST structure, the Arctic SIC decline centered over the Barents–Kara Seas and Baffin Bay, the corresponding T2M warming pattern, and the multidecadal evolution of the CCA2 time series support the interpretation of this pair as an AMO-related mode of Arctic winter variability.

Interannual footprints on Arctic coupled SIC-T2M-SLP fields

The SST pattern of CCA3 (8.8%; Fig. 3a) shows negative SST anomalies over the subpolar gyre (Fig. 3a), while positive anomalies are observed in the western subtropical North Atlantic and near the eastern US coastline. This tripolar pattern has been previously linked to interannual atmospheric variability[43,58–60]. The Arctic SIC pattern of CCA3 (Fig. 3c) explains 7.7% of SIC variance and exhibits a dipole-like structure: reduced SIC across the Barents–Kara Seas, the Greenland and Norwegian Seas, accompanied by increased SIC over Baffin Bay and the Labrador Sea. Reduced SIC in the Barents–Kara region and along the Eurasian Arctic coast has been previously documented in connection with interannual variability[60–62], while positive SIC anomalies in Baffin Bay and the Labrador Sea are consistent with earlier results linking Atlantic atmospheric variability to enhanced cold air advection and regional winter ice accumulation[63,64].

The T2M pattern of CCA3 (5.0% of variance explained; Fig. 3d) also exhibits a pronounced dipole across the Arctic domain. Strong positive anomalies extend over northern Eurasia and the Barents–Kara sector, while negative temperature anomalies dominate the western Arctic, including Greenland, the Canadian Arctic Archipelago, and the Beaufort–Chukchi region. Unlike the thermodynamic responses seen in CCA1 and CCA2, the strongest T2M loadings in CCA3 are not co-located with the regions of strongest SIC anomalies. Instead, this pattern reflects large-scale continental advection, with enhanced westerly flow transporting warmer air into Eurasia and cooler Arctic-origin air toward Baffin Bay and the Canadian Arctic Archipelago. The SLP field associated with CCA3 (Fig. 3e) displays strong positive anomalies extending over the mid-latitude North Atlantic and western Europe, while negative anomalies dominate the Arctic and subpolar regions. The North Atlantic SST structure, the SIC dipole with intense loadings over the Atlantic Arctic sector and Baffin Bay, and the corresponding T2M dipole suggest that this pair is related to Atlantic atmospheric variability. The time series of this pair (Fig. 3b) shows mainly interannual variability, but also a weak trend during some periods. To assess the temporal relationship between CCA3 and Atlantic atmospheric variability, we compared the CCA3 time series with the North Atlantic Oscillation[59] (NAO), Arctic Oscillation[65] (AO) and East Atlantic Pattern[66] (EA) indices (Fig. S1). Over the full 1950–2024 period, the PC3 detrended correlations are strongest for NAO ($r = 0.40$), followed by AO ($r = 0.32$), while EA is weaker ($r = 0.18$). These relationships change across subperiods: AO has the strongest correlation with CCA3 during 1950–1975, EA becomes relatively more prominent during 1975–2000, and NAO becomes the strongest correlate during 2000–2024 (Fig. S1b). Therefore, CCA3 is not interpreted as a single-driver mode, but rather as a broader Atlantic atmospheric circulation mode.

With CCA4, we identify another coupled mode dominated by interannual variability. The SST pattern of CCA4 (9.7% of variance explained; Fig. 4a) is characterized by positive anomalies across the central and eastern equatorial Pacific together with negative anomalies in the western tropical Pacific and North Pacific subtropics, closely matching the canonical El Niño-Southern Oscillation[67,68] (ENSO) pattern. The Arctic SIC pattern of CCA4 (4.0% of variance explained; Fig. 4c) shows strong negative anomalies around Ellesmere Island, the Canadian Arctic Archipelago, and Baffin Bay, extending into the Greenland Sea. This is consistent with findings that show El Niño conditions are linked to decreased SIC and increased T2M across the Canadian–Greenland sector[24]. In contrast, positive SIC anomalies appear over the North Pacific

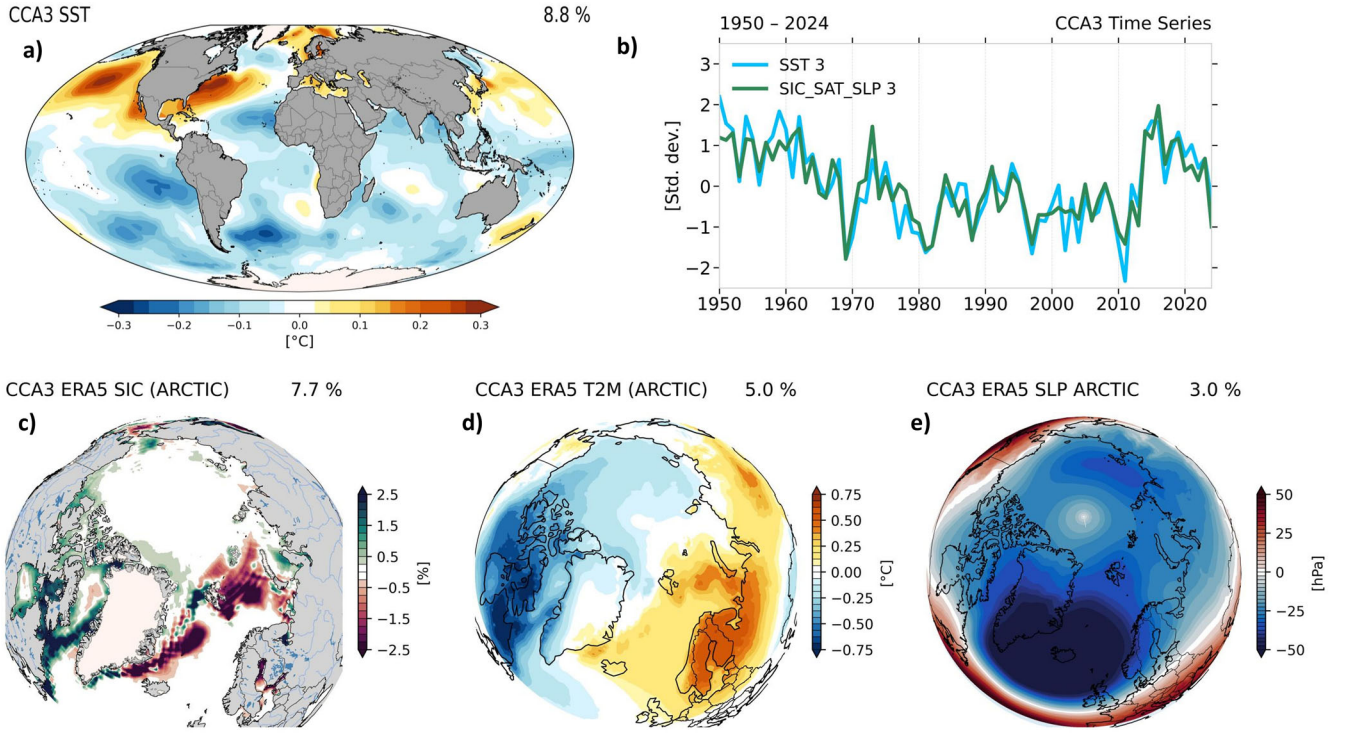

Fig. 3 | Third coupled pair of global SST (ERSSTv5) and Arctic SIC, T2M, and SLP (ERA5) October–March anomalies from 1950 to 2024. The SST spatial structure of the third CCA pair (**a**), explaining 8.8% of variance, together with coupled Arctic SIC (**c**; 7.7% of variance), T2M (**d**; 5.0% of variance), and SLP (**e**; 3.0% of variance) fields north of 50° N for SIC and T2M, and north of 40° N for SLP. The correlation between their corresponding time series (**b**) is 0.91.

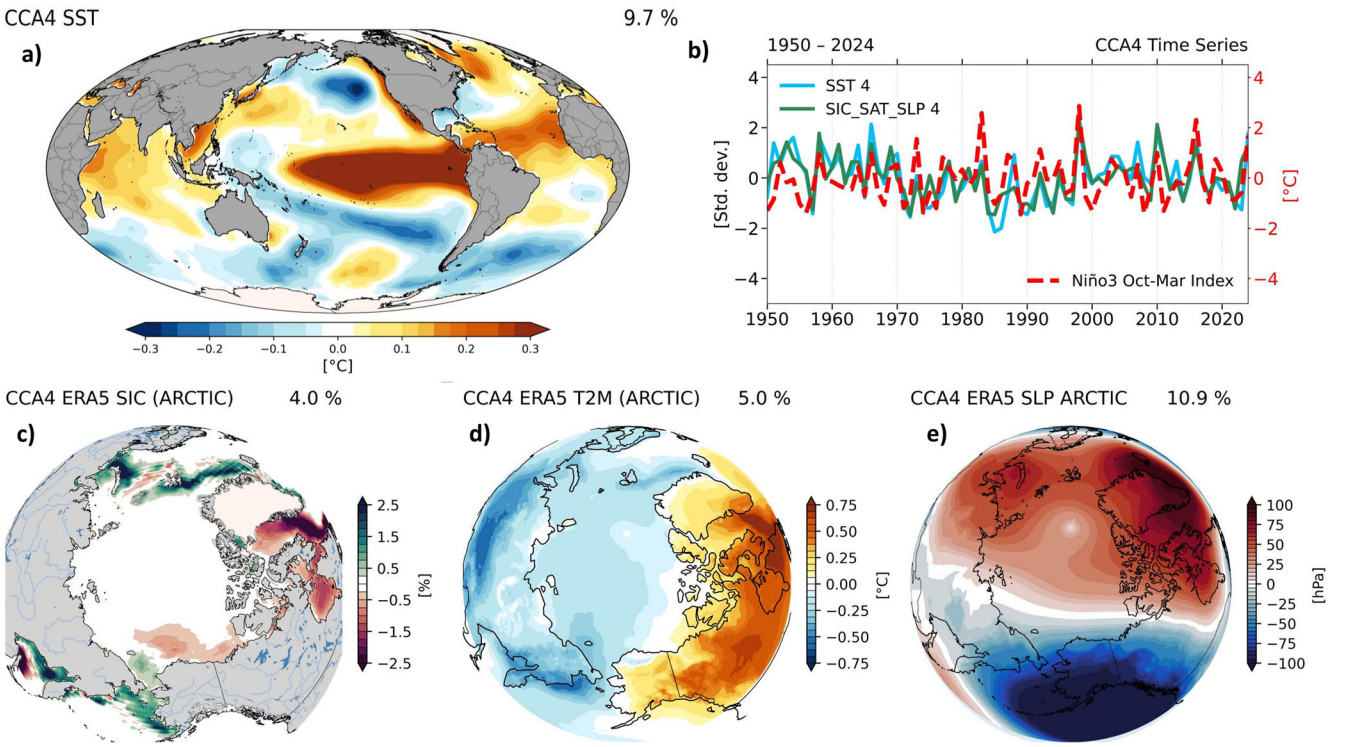

Fig. 4 | Fourth coupled pair of global SST (ERSSTv5) and Arctic SIC, T2M, and SLP (ERA5) October–March anomalies from 1950 to 2024. The SST spatial structure of the fourth CCA pair (**a**), explaining 9.7% of variance, together with coupled Arctic SIC (**c**; 4.0% of variance), T2M (**d**; 5.0% of variance), and SLP (**e**; 10.9% of variance) fields north of 50° N for SIC and T2M, and north of 40° N for SLP. The correlation between their corresponding time series (**b**) is 0.89. Their correlation with the Niño3 Index (red line) is 0.54 (95% confidence level).

Arctic sector, matching the tendency for increased SIC in the Pacific sector due to changes in the Aleutian Low[69,70]. The SIC pattern of this pair also exhibits a dipole-like structure similar to that identified in the CCA3 SIC, with opposite loadings over Baffin Bay and the Barents–Kara Seas, which is consistent with previous work showing that ENSO can influence Barents-Kara Seas winter sea ice through an Atlantic pathway involving atmospheric circulation anomalies[71]. The T2M pattern of CCA4 (5.0%; Fig. 4d) exhibits a pronounced Pacific–North American–Arctic temperature dipole[25], with strong positive anomalies over northern Canada, Ellesmere Island, and Hudson Bay, co-located with regions of reduced SIC. The SLP field of CCA4 (10.9%; Fig. 4e) displays a marked Arctic dipole structure, with a deepened Aleutian Low over the North Pacific and positive SLP anomalies centered over the Canadian Arctic and Greenland. This pattern is a well-established extratropical response to ENSO[24,69,70]. The time series of this pair (Fig. 4b) are significantly correlated with Niño3 Index ($r = 0.54$, 95% confidence level). The tropical Pacific SST structure of this pair, the Arctic SIC–T2M-SLP footprint consistent with previous studies, and the significant correspondence with the Niño3 Index support the interpretation of CCA4 as an ENSO-related mode of Arctic winter interannual variability.

Causal links from anthropogenic and internal drivers to Arctic SIC

CCA does not provide any information about causality between different patterns and their attributed drivers. To move beyond correlation-based inferences and assess whether the large-scale drivers inferred from CCA exert a causal influence on Arctic SIC, we therefore analyze CCM together with IF, two methods that explicitly quantify causality between different pattern changes. To ensure consistency with the CCA framework, and increase the signal to noise ratio, all causal maps are computed using the Arctic winter SIC field reconstructed from the leading 8 EOFs. In order to support the attribution of the CCA pairs we first use CCM to test for a causal relationship from GW Index to CCA1 (Fig. 5a), AMO Index to CCA2 (Fig. 5b), and Niño3 Index to CCA4 (Fig. 5c). For all three indices, we find a significant causal signal, where cross-map skill increases monotonically with library size and stabilizes well above the 95% confidence level envelopes of both Ebisuzaki[72] and bootstrap surrogates (see Methods for details). We find the strongest convergence for the GW-related CCA pair and for ENSO, followed by AMO. Because CCA3 is interpreted as a broader Atlantic atmospheric circulation mode, we compared the CCA3 time series with several interannual atmospheric indices, including NAO, AO, EA, and Niño3 (Fig. S2). These tests show detectable but weaker convergence for NAO (Fig. S2a) and AO (Fig. S2b), while EA (Fig. S2c) and Niño3 (Fig. S2d) remain within the surrogate envelopes and do not show robust convergence. Similar CCM analyses reveal significant causal links from the same indices to the CCA SST time series (Fig. S3). Time-delay CCM analysis supports the inferred direction of causality, with peak cross-map skill occurring at negative or near-zero lags (Fig. S4), consistent with a driver to response relationship rather than a reversed association.

In a second, CCA-independent step, we apply CCM directly between each of the four indices and the Arctic winter SIC anomalies, thereby mapping regions where each driver exerts a robust causal influence on SIC variability. The GW Index shows widespread and spatially coherent cross-map skill along both the Atlantic and Pacific marginal ice zones (Fig. 6a), particularly over the Greenland Sea, Barents–Kara Seas, Chukchi Sea, and Beaufort Sea. The AMO Index shows a similar but more regional footprint (Fig. 6b), with the strongest and most consistent cross-map skill over the Greenland Sea and Baffin Bay. The difference between Fig. 6a and Fig. 6b, in line with CCA1 (Fig. 2a) and CCA2 (Fig. 2c) SIC patterns, supports the attribution and separation of anthropogenic warming (CCA1) from multidecadal Atlantic variability (CCA2). The IF map from the Global Warming Index to winter Arctic SIC field (Fig. 6c) also reveals strong and statistically significant directed information transfer across much of the Arctic marginal ice zone, confirming the spatially coherent and basin-scale imprint of the anthropogenic mode identified in CCA1. In contrast, the IF map for AMO (Fig. 6d) shows significant but spatially confined influence, primarily over the Greenland Sea and Baffin Bay. For Niño3 Index, the CCM map (Fig. S5b) shows significant influence over the North Pacific sector, the Canadian–Greenland sector, and Hudson Bay, a pattern consistent with the main SIC loadings of CCA4 but only partly reproduced by the IF map (Fig. S5d). Thus, while the causal maps are less spatially robust than those for GW and AMO, they remain physically consistent with the CCA4 SIC structure (Fig. 4c) and with the Niño3 → CCA4 CCM result (Fig. 5c). For transparency, we also retain the corresponding CCM and IF maps obtained from the SIC field without the 8-EOF reconstruction in Fig. S6.

Physical links from anthropogenic and internal drivers to Arctic SIC

To explicitly diagnose how Arctic SIC, T2M, SST, and atmospheric circulation interact within each CCA mode, we analyze composite differences (high minus low PC years; Oct–Mar, 1950–2024) of upward turbulent heat flux (sensible + latent), downward longwave radiation, and 850-hPa geopotential height (Z850) with winds (Fig. 7). For CCA1, the regions of strongest winter SIC decline, especially Baffin Bay, Greenland Sea, Barents–Kara Seas, and Chukchi Sea, are co-located with enhanced upward turbulent heat flux and increased downward longwave radiation (Fig. 7a, e), indicating strong local thermodynamic coupling. This coupling is consistent with previous work showing that winter Arctic amplification is tightly linked to SIC loss and associated ocean-to-atmosphere heat release, with surface fluxes and longwave feedbacks maximizing in the cold season rather than at the time of maximum summer SIC retreat[29,31]. Over Baffin Bay, the Z850 and wind anomalies (Fig. 7i) indicate cold air advection from the Arctic, which in isolation would favor increased SIC. However, SIC still declines there, consistent with the strong local surface-energy anomalies seen in the flux and radiation diagnostics. Thus, in CCA1, thermodynamic forcing appears to dominate the SIC response even where the circulation anomaly would otherwise favor increased sea ice.

For CCA2, increased upward turbulent heat flux and downward longwave radiation are confined mainly to the Barents–Kara Seas and Baffin Bay (Fig. 7b, f), consistent with the more regional and lower-amplitude SIC and T2M anomalies relative to CCA1. This suggests that thermodynamic coupling remains important in CCA2 but is spatially restricted. The composite difference map of upper-ocean heat content for CCA2 (Fig. S7) shows positive anomalies across much of the North Atlantic–Arctic SIC sector, including the Barents–Kara Seas and Baffin Bay, consistent with multidecadal oceanic influence contributing to the regional SIC decline in this pair[53,55]. By contrast, SIC anomalies in the Beaufort Sea and Canadian Arctic Archipelago sectors are not accompanied by comparably strong local surface-flux amplification. Instead, a broad positive Z850 center over the North Pacific (Fig. 7j) favors warm air advection into these regions, supporting regional SIC decline[73]. For CCA3, turbulent heat-flux anomalies are weak and spatially limited (Fig. 7c), while downward longwave radiation exhibits a dipole structure that mirrors the SIC dipole (Fig. 7g). The Z850 and wind anomalies (Fig. 7k) instead indicate strong horizontal temperature advection, with warm air transported into the Greenland and Barents–Kara Seas and cold Arctic air advected into Baffin Bay and the Labrador sector[60–62]. This circulation-driven forcing explains the opposing SIC and T2M anomalies without the strong local thermodynamic amplification characteristic of CCA1. In this sense, the CCA1–CCA3 contrast illustrates that similar circulation patterns can produce fundamentally different Arctic SIC responses depending on whether local surface-energy feedbacks or dynamical advection dominate the mode. For CCA4, turbulent heat-flux anomalies (Fig. 7d) show positive values over the North Pacific, contrasting with the positive SIC anomalies (Fig. 4c), while downward longwave-radiation anomalies are weak across most of the Arctic, including regions where pronounced SIC anomalies occur (Fig. 7h). However, the Z850 and 850-hPa wind anomalies (Fig. 7l) show significant Z850 anomalies over the North Pacific/Aleutian Low region and the opposite Arctic–North American sector. This circulation pattern generates warm air advection into the Canadian Arctic Archipelago and Hudson Bay, where SIC is reduced

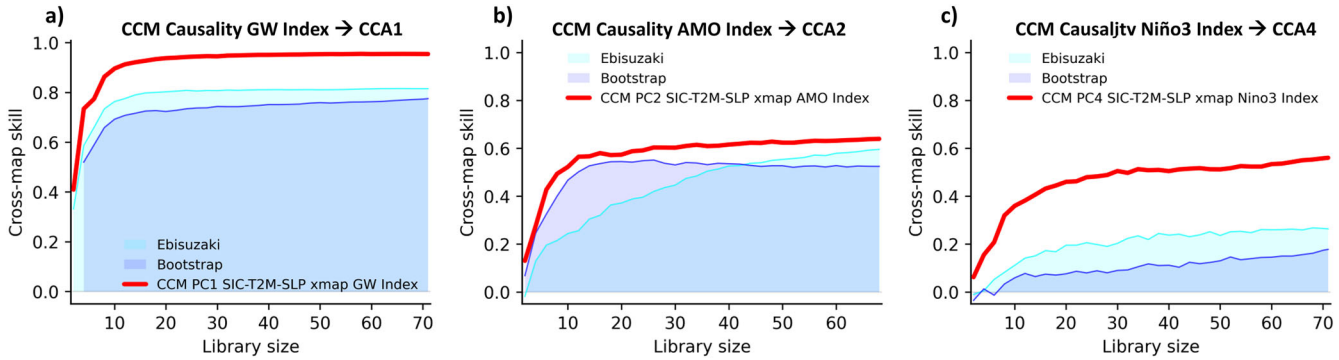

Fig. 5 | CCM evidence for causal links between major climate drivers and coupled SIC-T2M-SLP pairs derived from CCA. Cross-map skill as a function of library size for Global Warming (GW) Index → CCA1 (**a**), AMO Index → CCA2 (**b**), and Niño3 Index → CCA4 (**c**). Red curves denote CCM cross-map skill, while cyan and blue shaded envelopes indicate the 95% confidence ranges estimated from Ebisuzaki phase-randomised surrogates and bootstrap resampling, respectively.

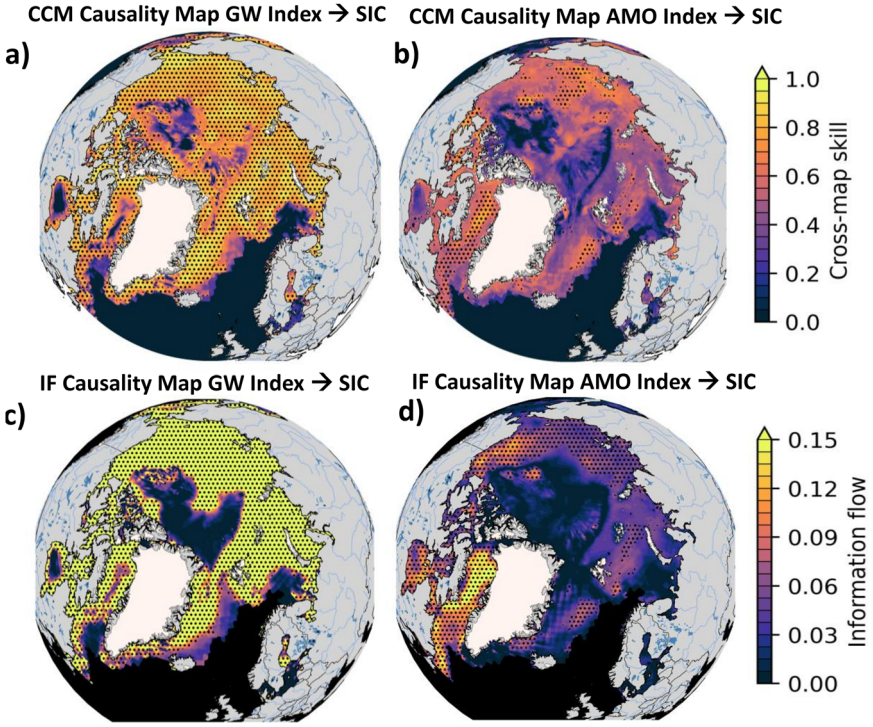

Fig. 6 | Spatial causal maps of major climate drivers on Arctic winter SIC. a, **b** CCM cross-map skill from the Global Warming (GW) Index and AMO Index to Arctic winter sea-ice concentration (SIC), respectively. Colors denote CCM cross-map skill, and stippling marks grid points exceeding the 95% confidence level based on surrogate testing. **c**, **d** Corresponding IF maps showing directed information transfer from the GW Index and AMO Index to SIC. Colors indicate the magnitude of information flow (non-negative), and stippling denotes grid points significant at the 95% confidence level. SIC field was first reconstructed from the leading eight EOFs prior to the causal analysis.

(Fig. 4c), and cold air advection toward the Chukchi/North Pacific sector, where SIC in CCA4 slightly increases. SIC anomalies in this pair are therefore interpreted primarily as a circulation-driven ENSO response[24,69,70] rather than as a response to strong local surface-energy feedbacks.

Discussion

Using a coupled SST–Arctic SIC–T2M–SLP framework, we separate observed winter Arctic variability into a dominant global warming mode, a multidecadal Atlantic mode, and two modes linked primarily to interannual variability from Atlantic and Pacific realms. The attribution of each CCA mode is not based on a single diagnostic, but on convergent evidence from the global SST structure, the temporal behavior of the CCA time series in relation to the associated index and the consistency of these patterns with known physical mechanisms. CCA1 combines a quasi-uniform global SST warming pattern, basin-wide Arctic SIC decline with amplified T2M warming and a time series that closely follows the Global Warming Index. CCA2 is distinguished from CCA1 by its Atlantic-centered multidecadal SST structure and its regional Arctic footprint, with strongest SIC and T2M anomalies over the Barents–Kara Seas and Baffin Bay. In contrast, the third and fourth CCA pairs, which are governed primarily by large-scale circulation anomalies, generate opposing SIC and T2M responses across the Arctic. CCA-pair attribution is independently supported by the causal diagnostics. CCM analysis between each driver index and the corresponding CCA time series indicates robust convergence for all four modes, confirming that the temporal evolution of the CCA patterns is consistent with directional forcing from the corresponding drivers. The clearest causal footprint on winter Arctic SIC is found for the Global Warming Index, which shows widespread and spatially coherent influence along the Arctic marginal sea ice zone whereas the AMO-linked pair shows a more regional Atlantic-sector footprint, particularly over the Barents–Kara Seas and Baffin Bay. For ENSO, the causal signals are strong at the index to CCA time series level, but weaker and less spatially extensive. However, they remain physically consistent with the SIC structures of CCA4. The weaker and less spatially extensive ENSO signal in the SIC causal maps likely reflects the intermittent and circulation mediated nature of ENSO teleconnections into the Arctic.

Physical diagnostics provide the final line of support for this interpretation. In CCA1 and, to a lesser extent, CCA2, regions of winter SIC

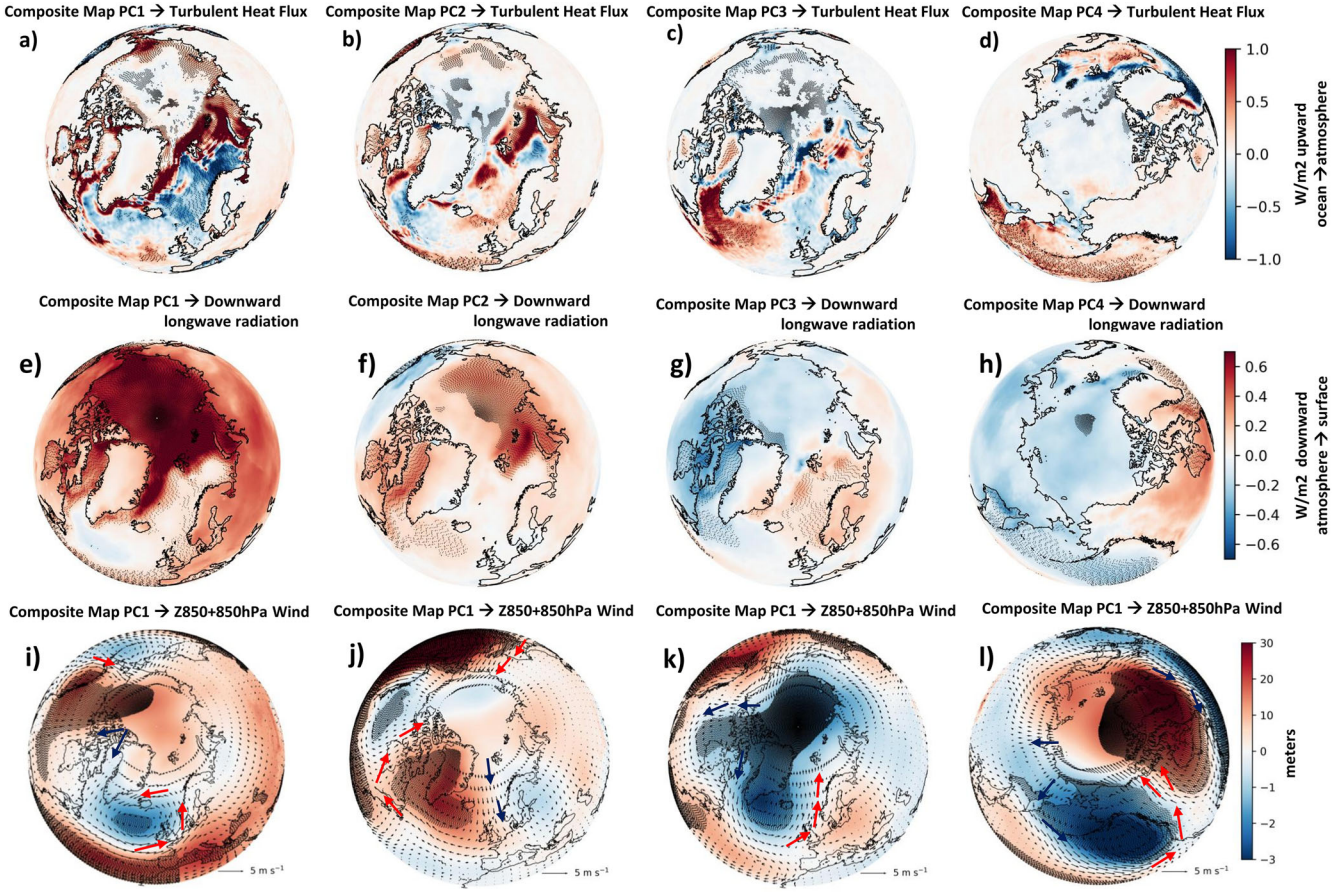

Fig. 7 | Thermodynamic and dynamical coupling diagnostics for CCA 1–4 (Oct–Mar, 1950–2024). a–d Upward turbulent heat flux composite difference (high minus low PC years; sign convention: ocean→ atmosphere positive). Stippling denotes grid points significant at the 95% confidence level. **e–h** Downward longwave radiation (STRD) composite difference (atmosphere→surface positive). Stippling denotes grid points significant at the 95% confidence level. **i–l** Z850 composite difference with 850-hPa wind anomalies. Stippling denotes grid points significant at the 95% confidence level; vectors are plotted south of 84°N for clarity.

decline are co-located with enhanced upward turbulent heat flux and increased downward longwave radiation, indicating strong thermodynamic coupling between SIC loss and lower-tropospheric warming. In contrast, CCA3 and CCA4 are dominated more clearly by lower tropospheric circulation and horizontal temperature advection, with comparatively weak local surface flux anomalies. This contrast explains why similar large-scale circulation patterns can produce different SIC and T2M responses across modes, and why weak SLP variance in the leading modes should not be interpreted as evidence of weak physical coupling. Rather, it reflects the fact that the anthropogenic and AMO-related influence are expressed primarily through local surface-energy feedbacks, whereas the interannual modes operate more strongly through dynamical atmospheric forcing. Our results are broadly consistent with other studies of Arctic SIC variability based on similar statistical methods[9,15,16,19,74], including Low-Frequency Component Analysis[33], that also identified a dominant forced component together with distinct regional internal modes.

Regional trend quantification suggests where the leading coupled modes account for the observed Arctic winter SIC decline (Fig. S8). Prior to about 1980, regional SIC anomalies fluctuate substantially but did not exhibit a persistent, pan-Arctic declining tendency (Fig. S8a). After 1980, CCA1 and CCA2 together explain a large fraction of the observed 1980–2024 winter SIC trend across more regions, including about 81% in the Beaufort Sea–Canadian Arctic Archipelago, 77% in the Greenland Sea, 71% in the East Siberia–Laptev Seas, 63% in the Chukchi Sea, and 58% in the Baffin Bay–Labrador Sea sector (Fig. S8b). The main exception is the Barents–Kara Seas, where the observed decline is very large but CCA1 and CCA2 together capture only about 31% of the trend, suggesting that additional regional feedbacks or forcings amplify the SIC trend there beyond what is represented by the two leading CCA pairs. Over the Greenland Sea, the trend spatial pattern (Fig S8b) suggests a superposition of strong negative trend signals with localized weak positive trend, likely due to sea ice advection through Fram Strait associated with AMO variability, which can partially counteract thermodynamically driven losses from CCA1. The relative impact of the two CCA pairs is also different in each SIC sector (Fig. S8c), with CCA1 exceeding CCA2 in all regions except Baffin Bay–Labrador Sea, where the AMO-related contribution is slightly larger, indicating an especially strong influence of multidecadal Atlantic variability there.

A growing body of work has linked Arctic sea ice decline to intensified mid-latitude extreme events[7,75–78], showing that large-scale reductions in SIC weaken the meridional temperature gradient, alter the jet stream, and promote the development of persistent summer blocking over Europe[78–80] that favor clear-sky, subsident, and radiatively driven summer heatwaves[81]. However, in most of these studies the decline in Arctic SIC is treated as a single, monolithic forcing, irrespective of its origin and the nature of the causal link to external or internal drivers. As a downstream implication, we examined whether the winter coupled Arctic modes project onto subsequent European summer daily maximum temperature (TX) variability (Fig. S9). The anthropogenically induced SIC decline (CCA1) is associated with a broad warm-season TX signal over much of Europe (Fig. S9a), whereas the AMO-related mode (CCA2) exhibits a much weaker and confined response over Eastern Europe (Fig. S9d). Consistent with this contrast, causality maps indicate a clearer downstream influence for CCA1 (Fig. S9b, c) than for CCA2 (Fig. S9e, f). Both CCA3 and CCA4 are associated with SIC patterns characterized by alternating positive and negative anomalies across the Arctic and therefore lack a coherent and spatially integrated signal and they do not generate a consistent downstream

response in summer European TX (Fig. S10). We do not interpret TX loadings over Russia, Turkey, and Northern Africa due to known data limitations over these regions[82]. We also emphasize that these results should be interpreted as the projection of the winter coupled SST–SIC–SLP Arctic state onto later warm season variability, rather than as evidence that SIC decline alone drives European summer extremes. A full mechanistic attribution of this lagged connection would require dedicated analyses of the intervening circulation pathways, such as atmospheric blocking, jet variability, and stratosphere–troposphere coupling[28,78,83].

The separation of anthropogenic influence from interannual and multidecadal internal variability is essential for interpreting recent trends, understanding regional patterns of winter Arctic amplification and downstream influence on European extreme events. These results highlight the importance of viewing Arctic winter sea ice not as a single, uniformly declining field, but as the superposition of multiple physical processes operating on different spatial and temporal scales. This framework can in principle also be applied to output from climate simulations, thereby exploiting the ability of climate models to extend analysis beyond the relatively short observational record, and to trace changes in sea ice via statistical and causal relationships in distant past or future climate states. Upcoming generations of both highly efficient and high-resolution climate models will provide valuable opportunities to further investigate the mechanisms identified here, particularly as very high-resolution simulations become available through CMIP7 and related model intercomparison efforts.

Methods

Data

We use monthly Extended Reconstructed Sea Surface Temperature v5[84] (ERSSTv5; NOAA), a global, homogenized SST product suited for long-term variability and low-frequency climate analysis (https://psl.noaa.gov/data/gridded/data.noaa.ersst.v5.html). ERSSTv5 is based on in situ measurements and statistical reconstruction techniques and provides a stable record from the mid-twentieth century onward. Sea ice concentration data is obtained from the fifth generation European Centre for Medium-Range Weather Forecasts (ECMWF) Reanalysis (ERA5), at 0.25° × 0.25° spatial resolution(https://cds.climate.copernicus.eu/cdsapp#!/dataset/reanalysis-era5-single-levels-monthly-means?tab=form). The ERA5R is the state-of-the-art reanalysis produced by the ECMWF and provides a variety of atmospheric and climate variables[85]. From ERA5, we also used sea level pressure, two-meter temperature (T2M), geopotential height (Z850) together with zonal and meridional wind at 850 mb, upward turbulent heat flux (sensible + latent) and downward longwave radiation. Daily maximum temperature (TX) is taken from the E-OBS[82] observational dataset (version 29.0e), covering the 1950–2023 period at 0.1° × 0.1° resolution(https://cds.climate.copernicus.eu/datasets/insitu-gridded-observations-europe?tab=overview). The dataset is produced by the Copernicus Climate Change Service and is based on station measurements that are quality-controlled and interpolated onto a regular grid. All fields are first converted to monthly anomalies relative to the 1980–2010 climatology. To construct a single winter value for each year, we use October–March means, where the October–December months belong to the preceding calendar year. For example, the winter of 1950 is defined from October–December 1949 and January–March 1950. For TX, we use May–September (MJJAS) averages to characterize summer conditions.

Climate indices

The Global Warming (GW) Index is constructed from ERA5 data by averaging the global T2M anomalies over all grid points. The Atlantic Multidecadal Oscillation (AMO) index is obtained from NOAA (https://psl.noaa.gov/data/timeseries/AMO/) and is defined as the detrended SST anomaly averaged over the North Atlantic basin (0°–70° N). The Arctic Oscillation, North Atlantic Oscillation and East Atlantic Index are taken from the NOAA Climate Prediction Center (https://www.ncei.noaa.gov/access/monitoring/). The Niño3 Index used here is retrieved from NOAA (https://psl.noaa.gov/data/timeseries/month/Nino3/) and represents the monthly SST anomaly averaged over 5°S–5°N and 150°W–90°W. For all indices, we compute October–March means to match the winter definition used for SST, SIC, T2M and SLP.

Canonical Correlation Analysis (CCA)

CCA[35] is a multivariate statistical technique used to identify coupled modes between global SST and the Arctic coupled SIC, T2M and SLP fields. CCA provides pairs of spatial patterns whose associated time series (canonical variates) exhibit maximum correlation, while successive pairs remain mutually orthogonal. CCA estimates two sets of canonical vectors, solved through the generalized eigenvalue problem of the cross-covariance matrices. Before applying CCA, each field is reduced through EOF analysis to avoid degeneracy of the covariance matrices. We retain the leading eight EOF modes explaining ~70% of variance in each field[86]. Their PC time series form the two input matrices (X for SST and Y for SIC–T2M–SLP). CCA then solves the generalized eigenvalue problem for the cross-covariance matrices of X and Y, yielding two sets of canonical vectors (one for each field). The canonical time series are obtained by projecting the reconstructed fields onto their corresponding canonical vectors. The resulting pairs represent distinct, maximally coupled modes of co-variability. For each canonical mode k, spatial loading patterns are obtained by regressing the standardized canonical time series $a_k(t)$ onto the original anomaly field $F(\mathbf{x}, t)$. At each grid point, the local fraction of variance explained by mode kis computed as the squared Pearson correlation coefficient:

$$R_k^2(\mathbf{x}) = \mathrm{corr}^2\left(F(\mathbf{x}, t), a_k(t)\right) \quad (1)$$

The resulting pairs represent distinct, maximally coupled modes of co-variability. This quantity represents the proportion of temporal variance at grid point **x**that is linearly associated with the canonical mode. The regional percentage of variance explained reported in the manuscript is then obtained by spatially averaging $R_k^2(\mathbf{x})$ over the analyzed domain. This measure quantifies the mean local variance explained by a given coupled mode and is computed separately for each variable. The canonical modes are ordered according to decreasing canonical correlation between the paired time series, not according to the variance explained in any individual field. CCA has been previously successfully used in climate research to identify links between large scale patterns in key climate variables, like atmospheric circulation, temperature, sea ice or clouds[14,41,81,86,87] and can provide similar results to Low-Frequency Component Analysis (LFCA) analysis[33], a method that maximizes low-frequency variance within a combined state vector. However, our CCA framework maximizes coupling between global SST and the Arctic SIC–T2M–SLP state and therefore the two approaches are complementary and need not yield an identical mode correspondence.

Convergent Cross Mapping (CCM)

CCM[36] is a causality-detection method grounded in dynamical systems theory. CCM reconstructs the system's state space using time-lagged embeddings of one variable and evaluates whether this reconstructed manifold can reliably estimate another variable. If X causes Y, then the reconstructed states of Y contain recoverable information about X. Cross-map skill is quantified as the correlation between predicted and observed values and must increase with library length (convergence) for the causal link to be distinguished from mere correlation. In this study, CCM is applied in two ways. First, we test causality between each climate index and the canonical time series associated with the CCA modes by cross-mapping the index from the corresponding PC series. A robust causal relationship is confirmed if the cross-map skill peaks at zero or negative lag, clearly identifying the direction of influence, the cross-map skill consistently increases and stabilizes as the library size increases (convergence criterion) and cross-map skill significantly exceeds the surrogate-based 95% confidence intervals. For this analysis, the optimal embedding dimension (E) and lag were determined using Time-Delay CCM[88] (TDCCM). The selected parameters are $E = 5$ and lag = −1 for GW–PC1, $E = 5$ and lag = -4 for AMO–PC2, and $E = 5$ and lag = −2 for ENSO–PC4. All selected lags satisfy the requirement

$|\text{lag}| \le E - 1$ and are used solely to maximize cross-map skill. Second, we perform CCM grid-point-wise on the winter SIC field: for each index, the index time series is cross-mapped from the SIC anomaly time series at every grid cell, yielding spatial maps of causal influence. The embedding lag is chosen to be 1 for all analyses. Statistical significance is assessed using surrogate time series built under two models: (1) Ebisuzaki[72] phase shift, which randomizes the phases of the time series, but keeps the same frequency spectrum and (2) Bootstrap surrogates, which resample a contiguous randomly chosen 10-point block of the original effect time series.

Information flow

The Information Flow[37] (IF) method estimates potential causal links between two time series by quantifying how much information is transferred from one to the other. The central quantity of interest is the information flow from X_1 to X_2, denoted $T_{1\to2}$, which is interpreted as a measure of the influence of X_1 on the evolution of X_2. Conceptually, $T_{1\to2}$, compares the total information in X_2 with the portion attributable to X_2's own independent fluctuations; if $T_{1\to2} = 0$, then X_1 provides no causal contribution to X_2. When $T_{1\to2} \neq 0$, and is statistically significant, its sign indicates the following: a positive $T_{1\to2}$, implies that X_1 increases the uncertainty of X_2 (i.e., makes X_2 less stable), whereas a negative $T_{1\to2}$, implies that X_1 reduces the uncertainty of X_2 (i.e., stabilizes X_2). Under this framework, the observed variability in X_2 can be viewed as arising from the contribution of information flow from X_1, X_2's intrinsic dynamics, and stochastic noise. Dividing $T_{1\to2}$, by the total variability of X_2 yields the relative information flow $\tau_{1\to2}$ (in %). It has been shown to perform well in certain nonlinear settings and has been widely applied to infer causal structure from observational data across fields such as climate science and economics.

Here we are interested in the spatial pattern of causality from one variable, X_1 to the field of a second variable X_2. To this end, we calculate the $T_{1\to2}$ (and $\tau_{1\to2}$) from the time series of X_1 to the time series at each grid point in the field of X_2 and thus obtain a causality map.

For both IF and CCM, the selected lags should be interpreted as statistical optima rather than physical propagation timescales. For CCM, optimal embedding dimension (E) is chosen as the Embedding which maximizes contemporaneous interactions and the lag is determined through time-delay CCM, the optimal lag is required to lie within the embedding window ($\text{lag} \le E-1$) and is chosen to maximize cross-map skill, but likewise it is not interpreted as a physical delay. Before applying CCM and IF, SIC field is reconstructed using the leading 8EOFs to increase the signal-to-noise ratio.

Regional trend decomposition and integrated pattern-impact metric. To quantify the contributions of individual CCA modes to regional winter (Oct–Mar) SIC change, we reconstruct the SIC anomaly field associated with each mode k as

$$\Delta\text{SIC}_k(t, \mathbf{x}) = \text{PC}_k(t)\text{regSIC}_k(\mathbf{x}), \tag{2}$$

where regSIC_k is the SIC regression/canonical pattern (expressed in SIC units) and $\text{PC}_k(t)$ is the corresponding standardized canonical time series. For each predefined region, we compute the area-weighted mean SIC time series from observations and from each reconstructed mode, and estimate linear trends over 1980–2024 (expressed as % per decade). Mode contributions to the regional trend are then given by the trends of the reconstructed regional series. The fraction of the observed trend captured by CCA1 + CCA2 is computed as $|T_{1+2}|/|T_{\text{obs}}|$ (reported as a percentage). In addition, we compute an integrated "pattern-impact" metric designed to summarize the regional leverage of each SIC canonical pattern on the 1980–2024 change. For each region and mode k, we calculate a regional structure strength

$$S_k = \sum\nolimits_{\mathbf{x}\in r} w(\mathbf{x})\left|\text{regSIC}_k(\mathbf{x})\right|, \tag{3}$$

using spherical/area weights $w(\mathbf{x})$. We then multiply this structure strength by the magnitude of the linear trend in $\text{PC}_k(t)$ over 1980–2024 to obtain a trend-weighted impact $I_k = S_k|\text{trend}(\text{PC}_k)|$. This metric retains the physical dimensions of a regional pattern leverage (up to a constant factor that is defined by PC normalization), and is used by us to compare the relative roles of CCA1 and CCA2 across regions.

Data availability

All data used in this study are publicly available from the sources listed in the "Methods" section.

Code availability

The codes used to generate the results in this study are publicly available on Zenodo: https://zenodo.org/records/19810861.

Received: 31 December 2025; Accepted: 12 May 2026;
Published online: 20 May 2026

References

1. Masson-Delmotte, V. et al. *Climate Change 2021: The Physical Science Basis* (Cambridge Univ. Press, 2021).
2. Chung, E.-S. et al. The role of sea ice in present and future Arctic amplification. *Commun. Earth Environ.* **6**, 910 (2025).
3. Smith, D. M. et al. The Polar Amplification Model Intercomparison Project (PAMIP) contribution to CMIP6: investigating the causes and consequences of polar amplification. *Geosci. Model Dev.* **12**, 1139–1164 (2019).
4. Pithan, F. & Mauritsen, T. Arctic amplification dominated by temperature feedbacks in contemporary climate models. *Nat. Geosci.* **7**, 181–184 (2014).
5. Sévellec, F., Fedorov, A. V. & Liu, W. Arctic sea-ice decline weakens the Atlantic Meridional Overturning Circulation. *Nat. Clim. Chang.* **7**, 604–610 (2017).
6. Nichita, D. R., Dubet, I., Dima, M. & Ionita, M. Tracing the observed causal impact of diminishing summer sea-ice concentration on the Atlantic Meridional Overturning Circulation. *Geophys. Res. Lett.* **52**, e2024GL113293 (2025).
7. Cohen, J. et al. Recent Arctic amplification and extreme mid-latitude weather. *Nat. Geosci.* **7**, 627–637 (2014).
8. Cohen, J. et al. Divergent consensuses on Arctic amplification influence on midlatitude severe winter weather. *Nat. Clim. Chang.* **10**, 20–29 (2020).
9. Vaideanu, P. et al. Interplay of anthropogenic and natural drivers of observed coupled sea surface temperature-Arctic sea ice variability. *Clim. Dyn.* **63**, 341–359 (2025).
10. Notz, D. & Stroeve, J. Observed Arctic sea-ice loss directly follows anthropogenic CO2 emission. *Science* **354**, 747–750 (2016).
11. Notz, D. & Stroeve, J. The trajectory towards a seasonally ice-free Arctic Ocean. *Curr. Clim. Change Rep.* **4**, 407–416 (2018).
12. Mueller, B. L., Gillett, N. P., Monahan, A. H. & Zwiers, F. W. Attribution of Arctic sea ice decline from 1953 to 2012 to influences from natural, greenhouse gas, and anthropogenic aerosol forcing. *J. Clim.* **31**, 7771–7787 (2018).
13. Cai, Q. et al. Accelerated decline of summer Arctic sea ice during 1850–2017 and the amplified Arctic warming during the recent decades. *Environ. Res. Lett.* **16**, 034008 (2021).
14. Vaideanu, P. et al. Large-scale sea ice-surface temperature variability linked to Atlantic meridional overturning circulation. *PLoS One* **18**, e0290437 (2023).
15. Cai, Q., Beletsky, D., Wang, J. & Lei, R. Interannual and decadal variability of Arctic summer sea ice associated with atmospheric teleconnection patterns during 1850–2017. *J. Clim.* **34**, 9931–9955 (2021).
16. Ionita, M. The Arctic winter seasons 2016 and 2017: Climatological context and analysis. *Climate* **11**, 43 (2023).
17. England, M., Jahn, A. & Polvani, L. Nonuniform contribution of internal variability to recent Arctic sea ice loss. *J. Clim.* **32**, 4039–4053 (2019).

18. Kerr, R. A. A North Atlantic climate pacemaker for the centuries. *Science* **288**, 1984–1985 (2000).
19. Deser, C. & Teng, H. Evolution of Arctic sea ice concentration trends and the role of atmospheric circulation forcing, 1979–2007. *Geophys. Res. Lett.* **35**, L02504 (2008).
20. Ding, Q. et al. Fingerprints of internal drivers of Arctic sea ice loss in observations and model simulations. *Nat. Geosci.* **12**, 455–460 (2019).
21. Olonscheck, D., Mauritsen, T. & Notz, D. Arctic sea-ice variability is primarily driven by atmospheric temperature fluctuations. *Nat. Geosci.* **12**, 449–454 (2019).
22. Wang, C. et al. Recent slowing of Arctic sea ice melt tied to multidecadal NAO variability. *Nat. Commun.* **16**, 1243 (2025).
23. Screen, J. A. & Deser, C. Pacific Ocean variability influences the time of emergence of a seasonally ice-free Arctic Ocean. *Geophys. Res. Lett.* **46**, e2018GL081798 (2019).
24. Clancy, R., Bitz, C. & Blanchard-Wrigglesworth, E. The influence of ENSO on Arctic sea ice in large ensembles and observations. *J. Clim.* **34**, 4457–4476 (2021).
25. Jeong, H., Park, H. S., Stuecker, M. F. & Yeh, S. W. Distinct impacts of major El Niño events on Arctic temperatures due to differences in eastern tropical Pacific sea surface temperatures. *Sci. Adv.* **8**, eabl8278 (2022).
26. Dai, A., Luo, D., Song, M. & Liu, J. Arctic amplification is caused by sea-ice loss under increasing CO2. *Nat. Commun.* **10**, 121 (2019).
27. Bushuk, M. et al. Predicting September Arctic sea ice: a multimodel seasonal skill comparison. *Bull. Am. Meteorol. Soc.* **105**, E1170–E1203 (2024).
28. Vihma, T. Effects of Arctic sea ice decline on weather and climate: a review. *Surv. Geophys.* **35**, 1175–1214 (2014).
29. Chung, E. S. et al. Cold-season Arctic amplification driven by Arctic Ocean-mediated seasonal energy transfer. *Earth's Future* **9**, e2020EF001772 (2021).
30. Huo, Y. et al. Changes in sea ice concentration explain half of the winter warming of the Arctic surface. *Commun. Earth Environ.* **6**, 91 (2025).
31. Deser, C., Tomas, R., Alexander, M. & Lawrence, D. The seasonal atmospheric response to projected Arctic sea ice loss in the late twenty-first century. *J. Clim.* **23**, 333–351 (2010).
32. Dörr, J., Årthun, M., Eldevik, T. & Madonna, E. Mechanisms of regional winter sea-ice variability in a warming Arctic. *J. Clim.* **34**, 7251–7270 (2021).
33. Dörr, J. S., Bonan, D. B., Årthun, M., Svendsen, L. & Wills, R. C. J. Forced and internal components of observed Arctic sea-ice changes. *Cryosphere* **17**, 4133–4157 (2023).
34. Chen, H. W., Alley, R. B. & Zhang, F. Interannual Arctic sea ice variability and associated winter weather patterns: A regional perspective for 1979–2014. *J. Geophys. Res. Atmos.* **121**, 10253–10273 (2016).
35. von Storch, H. & Zwiers, F. W. *Statistical Analysis in Climate Research*. https://doi.org/10.1017/CBO9780511612336 (Cambridge Univ. Press, 1999).
36. Sugihara, G. et al. Detecting causality in complex ecosystems. *Science* **338**, 496–500 (2012).
37. Liang, X. S. Information flow within stochastic dynamical systems. *Phys. Rev. E* **78**, 031113 (2008).
38. Dima, M., Nichita, D. R., Lohmann, G., Ionita, M. & Voiculescu, M. Early-onset of Atlantic Meridional Overturning Circulation weakening in response to atmospheric CO2 concentration. *npj Clim. Atmos. Sci.* **4**, 33 (2021).
39. Rahmstorf, S. et al. Exceptional twentieth-century slowdown in Atlantic Ocean overturning circulation. *Nat. Clim. Chang.* **5**, 475–480 (2015).
40. Burgard, C. & Notz, D. Drivers of Arctic Ocean warming in CMIP5 models. *Geophys. Res. Lett.* **44**, 4263–4271 (2017).
41. Vaideanu, P., Dima, M., Pirloaga, R. & Ionita, M. Disentangling and quantifying contributions of distinct forcing factors to the observed global sea level pressure field. *Clim. Dyn.* **54**, 1453–1467 (2019).
42. Dima, M. & Lohmann, G. A hemispheric mechanism for the Atlantic multidecadal oscillation. *J. Clim.* **20**, 2706–2722 (2007).
43. Deser, C., Alexander, M. A., Xie, S.-P. & Phillips, A. S. Sea surface temperature variability: patterns and mechanisms. *Annu. Rev. Mar. Sci.* **2**, 115–143 (2010).
44. Vaideanu, P., Dima, M. & Voiculescu, M. Atlantic Multidecadal Oscillation footprint on global high cloud cover. *Theor. Appl. Climatol.* **134**, 685–699 (2018).
45. Ruprich-Robert, Y. et al. Assessing the climate impacts of the observed Atlantic multidecadal variability using the GFDL CM2.1 and NCAR CESM1 global coupled models. *J. Clim.* **30**, 2785–2810 (2017).
46. Zhang, R. & Delworth, T. L. Impact of the Atlantic Multidecadal Oscillation on North Pacific climate variability. *Geophys. Res. Lett.* **34**, L23708 (2007).
47. Latif, M. et al. Reconstructing, monitoring, and predicting multidecadal-scale changes in the North Atlantic thermohaline circulation with sea surface temperature. *J. Clim.* **17**, 1605–1614 (2004).
48. Knight, J. R., Allan, R. J., Folland, C. K., Vellinga, M. & Mann, M. E. A signature of persistent natural thermohaline circulation cycles in observed climate. *Geophys. Res. Lett.* **32**, L20708 (2005).
49. Dima, M. & Lohmann, G. Evidence for two distinct modes of large-scale ocean circulation changes over the last century. *J. Clim.* **23**, 3276–3292 (2010).
50. Zhang, R. et al. Have aerosols caused the observed Atlantic multidecadal variability? *J. Atmos. Sci.* **70**, 1135–1144 (2013).
51. Otterå, O. H., Bentsen, M., Drange, H. & Suo, L. External forcing as a metronome for Atlantic multidecadal variability. *Nat. Geosci.* **3**, 688–694 (2010).
52. Mann, M. E., Steinman, B. A., Brouillette, D. J. & Miller, S. K. Multidecadal climate oscillations during the past millennium driven by volcanic forcing. *Science* **371**, 1014–1018 (2021).
53. Årthun, M., Eldevik, T., Smedsrud, L. H., Skagseth, O. & Ingvaldsen, R. B. Quantifying the influence of Atlantic heat on Barents Sea ice variability and retreat. *J. Clim.* **25**, 4736–4753 (2012).
54. Li, F., Orsolini, Y. J., Wang, H., Gao, Y. & He, S. Atlantic Multidecadal Oscillation modulates the impacts of Arctic sea ice decline. *Geophys. Res. Lett.* **45**, 1214–1223 (2018).
55. Miles, M. W. et al. A signal of persistent Atlantic multidecadal variability in Arctic sea ice. *Geophys. Res. Lett.* **41**, 463–469 (2014).
56. Smedsrud, L. H., Halvorsen, M. H., Stroeve, J. C., Zhang, R. & Kloster, K. Fram Strait sea ice export variability and September Arctic sea ice extent over the last 80 years. *Cryosphere* **11**, 65–79 (2017).
57. Ionita, M., Scholz, P., Lohmann, G., Dima, M. & Prange, M. Linkages between atmospheric blocking, sea ice export through Fram Strait and the Atlantic Meridional Overturning Circulation. *Sci. Rep.* **6**, 32881 (2016).
58. Visbeck, M. H., Hurrell, J. W., Polvani, L. & Cullen, H. M. The North Atlantic Oscillation: past, present, and future. *Proc. Natl. Acad. Sci. U.S.A.* **98**, 12876–12877 (2001).
59. Hurrell, J. W. Decadal trends in the North Atlantic Oscillation: regional temperatures and precipitation. *Science* **269**, 676–679 (1995).
60. Hurrell, J. W. & Deser, C. North Atlantic climate variability: the role of the North Atlantic Oscillation. *J. Mar. Syst.* **78**, 28–41 (2009).
61. Zhang, X., Ikeda, M. & Walsh, J. E. Arctic sea ice and freshwater changes driven by the atmospheric leading mode in a coupled sea ice-ocean model. *J. Clim* **16**, 2159–2177 (2003).
62. Strong, C. & Magnusdottir, G. Modeled winter sea ice variability and the North Atlantic Oscillation: A multi-century perspective. *Clim. Dyn.* **34**, 515–525 (2010).
63. Wang, J., Mysak, L. A. & Grant Ingram, R. Interannual variability of sea-ice cover in Hudson Bay, Baffin Bay and the Labrador Sea. *Atmos.-Ocean* **32**, 417–435 (1994).
64. Mysak, L. A., Ingram, R. G., Wang, J. & van der Baaren, A. The anomalous sea-ice extent in Hudson Bay, Baffin Bay and the Labrador Sea during three simultaneous NAO and ENSO episodes. *Atmos.-Ocean* **34**, 73–91 (1996).

65. Gong, D. & Wang, S. Definition of Antarctic Oscillation index. *Geophys. Res. Lett.* **26**, 459–462 (1999).
66. Comas-Bru, L. & McDermott, F. Impacts of the EA and SCA patterns on the European twentieth-century NAO-winter climate relationship. *Q. J. R. Meteorol. Soc.* **140**, 354–363 (2014).
67. McPhaden, M. J., Zebiak, S. E. & Glantz, M. H. ENSO as an integrating concept in Earth science. *Science* **314**, 1740–1745 (2006).
68. Philander, S. G. *El Niño, La Niña, and the Southern Oscillation* (Academic Press, 1990).
69. Alexander, M. A. et al. The atmospheric bridge: the influence of ENSO teleconnections on air-sea interaction over the global oceans. *J. Clim.* **15**, 2205–2231 (2002).
70. Bai, X. et al. Responses of surface heat flux, sea ice and ocean dynamics in the Chukchi-Beaufort Sea to storm passages during winter 2006/2007: a numerical study. *Deep-Sea Res. I* **102**, 1–13 (2015).
71. Luo, B. et al. Origins of Barents-Kara sea-ice interannual variability modulated by the Atlantic pathway of El Niño–Southern Oscillation. *Nat. Commun.* **14**, 2262 (2023).
72. Ebisuzaki, W. A method to estimate the statistical significance of a correlation when the data are serially correlated. *J. Clim.* **10**, 2147–2153 (1997).
73. Castruccio, F. S. et al. Modulation of Arctic sea ice loss by atmospheric teleconnections from Atlantic multidecadal variability. *J. Clim.* **32**, 1419–1443 (2019).
74. Deser, C., Walsh, J. E. & Timlin, M. S. Arctic sea ice variability in the context of recent atmospheric circulation trends. *J. Clim.* **13**, 617–633 (2000).
75. Sun, J., Liu, S., Cohen, J. & Yu, S. Influence and prediction value of Arctic sea ice for spring Eurasian extreme heat events. *Commun. Earth Environ.* **3**, 153 (2022).
76. Zhang, R., Sun, C., Zhu, J., Zhang, R. & Li, W. Increased European heat waves in recent decades in response to shrinking Arctic sea ice and Eurasian snow cover. *npj Clim. Atmos. Sci.* **3**, 15 (2020).
77. Ye, K. et al. Attributing climate and weather extremes to Northern Hemisphere sea ice and terrestrial snow: Progress, challenges and ways forward. *npj Clim. Atmos. Sci.* **8**, 82 (2025).
78. Vaideanu, P., Nichita, D. R., Boboc, L., Antonescu, B. & Ionita, M. An observation-based causal framework linking Barents-Kara sea ice to European heatwaves. *Environ. Res.: Climate* **5**, 015008 (2026).
79. Xu, M. et al. Distinct tropospheric and stratospheric mechanisms linking historical Barents-Kara sea-ice loss and late winter Eurasian temperature variability. *Geophys. Res. Lett.* **48**, e2020GL091791 (2021).
80. Mousavizadeh, M., Alizadeh, O., Hodges, K. I. & Simmonds, I. Causality in the winter interaction between extratropical storm tracks, atmospheric circulation, and Arctic sea ice loss. *J. Geophys. Res. Atmos.* **130**, e2024JD041203 (2025).
81. Ionita, M., Vaideanu, P., Nichita, D. & Nagavciuc, V. Breaking records under clear skies: The impact of sunshine duration and atmospheric dynamics on the 2024 Eastern European extreme summer temperatures. *npj Nat. Hazards* **2**, 82 (2025).
82. Cornes, R. C., van der Schrier, G., van den Besselaar, E. J. M. & Jones, P. D. An ensemble version of the E-OBS temperature and precipitation data sets. *J. Geophys. Res. Atmos.* **123**, 9391–9409 (2018).
83. Lee, D. Y. et al. The emergence of a dipole-like mode in Arctic atmospheric circulation conducive to European heat waves. *Commun. Earth Environ.* **6**, 700 (2025).
84. Huang, B. et al. Extended reconstructed sea surface temperature, version 5 (ERSSTv5): upgrades, validations, and intercomparisons. *J. Clim.* **30**, 8179–8205 (2017).
85. Hersbach, H. et al. The ERA5 global reanalysis. *Q. J. R. Meteorol. Soc.* **146**, 1999–2049 (2020).
86. Zorita, E., Kharin, V. & von Storch, H. The atmospheric circulation and sea surface temperature in the North Atlantic area in winter: their interaction and relevance for Iberian precipitation. *J. Clim.* **5**, 615–628 (1992).
87. Vaideanu, P., Ionita, M., Voiculescu, M. & Rimbu, N. Deconstructing global observed and reanalysis total cloud cover fields based on Pacific climate modes. *Atmosphere* **14**, 1181 (2023).
88. Ye, H., Deyle, E. R., Gilarranz, L. J. & Sugihara, G. Distinguishing time-delayed causal interactions using convergent cross mapping. *Sci. Rep.* **5**, 14750 (2015).

Acknowledgements

This work was supported by Helmholtz Association through the joint program "Changing Earth—Sustaining our Future" (PoF IV) program of the Alfred Wegener Institute Helmholtz Center for Polar and Marine Research (AWI) and by the project "Centre of Excellence for Climate and Societal Changes" (CECSC), number PN-IV-P6-6.1-CoEx-2024-0042 of the Romanian UEFISCDI. This work is also supported by the ERC grant "i2B" (grant no. 101118519), funded by the European Union. Views and opinions expressed are, however, those of the author(s) only and do not necessarily reflect those of the European Union or the European Research Council Executive Agency. Neither the European Union nor the granting authority can be held responsible for them. We acknowledge support by the Open Access publication fund of Alfred-Wegener-Institut Helmholtz Zentrum für Polar- und Meeresforschung.

Author contributions

P.V. and G.L. conceived the idea. P.V. and M.I. designed the methodology. P.V. and C.S. prepared the data. P.V. and D.R.N. analyzed the data. P.V., C.S., and M.I. prepared the figures. P.V. led the writing of the manuscript with significant input from M.I., C.S., D.R.N., M.D. and G.L.

Funding

Open Access funding enabled and organized by Projekt DEAL.

Competing interests

The authors declare no competing interests.

Additional information

Supplementary information The online version contains supplementary material available at https://doi.org/10.1038/s41612-026-01438-0.

Correspondence and requests for materials should be addressed to P. Vaideanu.